



Spatial frequency-based angular behavior of a short-range flicker-free MIMO–OCC link

SHIVANI RAJENDRA TELI,^{1,*}  STANISLAV ZVANOVEC,¹ RAFAEL PEREZ-JIMENEZ,²  AND ZABIH GHASSEMLOOY³ 

¹Department of Electromagnetic Field, Faculty of Electrical Engineering, Czech Technical University in Prague, Technicka, Prague 16627, Czech Republic

²IDeTIC, Universidad de Las Palmas de Gran Canaria, Las Palmas 35001, Spain

³Optical Communications Research Group, Faculty of Engineering and Environment, Northumbria University, Newcastle NE1 7RU, UK

*Corresponding author: telishiv@fel.cvut.cz

Received 3 August 2020; revised 8 October 2020; accepted 19 October 2020; posted 21 October 2020 (Doc. ID 404378); published 17 November 2020

In this paper, we provide a solution based on spatial frequency f_{sf} to study the angular behavior of a flicker-free, short-range indoor multiple-input multiple-output (MIMO) optical camera communications (OCC) link. We focus on the experimental investigation of OCC's performance for the transmitters (Tx) [i.e., light-emitting diode (LED) based arrays] located at the same and different distances from the receiver (Rx) with the off-axis rotation angle θ . We have used two 8×8 distributed LED arrays and a commercial low-cost complementary metal-oxide-semiconductor (CMOS) Raspberry Pi camera with the rolling-shutter capturing mode as the Tx and Rx, respectively. The image and the respective communications link quality metrics are measured in terms of the peak signal-to-noise ratio (PSNR) and the rate of successfully received bits with respect to f_{sf} for different camera shutter speeds (SS). A CMOS image sensor noise characterization is carried in terms of the signal-to-noise ratio (SNR) and PSNR. The proposed study provides a 100% success rate in data reception at the optimum θ of 50° at lower captured values of f_{sf} , which is projected onto the image sensor in the form of pixels. Moreover, the effect of channel saturation over f_{sf} is studied with respect to θ and SS and we show that, for θ exceeding the optimum value along transmission range, the f_{sf} area of the Tx reduces to less than $\sim 50\%$ of the captured Tx units at θ of 0° , where no data can be fully recovered. © 2020 Optical Society of America

<https://doi.org/10.1364/AO.404378>

1. INTRODUCTION

The rapid advances made in development of a range of complementary metal-oxide-semiconductor-based (CMOS-based) camera [image sensors (IS)], which are used in mobile phones (front/rear camera), digital single-lens reflex cameras with higher capture speeds [ranging from 30 to 1000 frames per second (fps)], and surveillance cameras, have recently motivated research and development in camera-based visible light communications (VLC), which is also known as optical camera communications (OCC) in the IEEE 802.15.7r1 Task Group [1,2]. The CMOS cameras can capture images or record videos in capturing modes based on global shutter (GS) and rolling shutter (RS) at different shutter speeds (SS) and resolutions.

In VLC links with transmitters (Tx) based on light-emitting diodes (LEDs), a wide range of dimming levels with no flickering can be adopted to ensure both illumination and data communications [3]. The IEEE 802.15.7 VLC standard outlines the maximum allowed flickering time period (MFTP) of 5 ms (i.e., 200 Hz) [4]. However, consumer-grade cameras

have a limited capture rate of approximately 60 fps. As a result, signals in OCC links can be captured at a very low sampling rate compared to the data transmission rate, thus resulting in the loss of unsampled data and a lower probability of signal detection. Moreover, OCC synchronization should be considered carefully by means of signaling, which reduces the data throughput [5]. Furthermore, a combination of LED-array Tx and OCC with a photodetector (PD) array can be used as massive multiple-input multiple-output (MIMO) to deliver parallel transmission and therefore higher data rates R_b in a range of applications, including the massive internet of things (IoT) [6,7]. Unlike the conventional PD-based Rx used in VLC, where the separation of mixed signals is not possible, the CMOS-based IS can capture lights coming from different directions and project them onto different sections of the IS (i.e., illuminating different PDs) [7]. Therefore, in these scenarios spatial separation of incoming light signals and their intensities can be determined by measuring the pixel value per light source images on the received frame. The data from the pixelated images can then be recovered from the

captured image frames using an image processing algorithm implemented in MATLAB, OpenCV, and Python [7]. In this approach, the CMOS IS can be used as the MIMO–OCC Rx without a need for extended hardware. For commercial use, a number of applications have been developed, including OCC for the automotive industry by Intel (USA) [8] and for an online-to-offline marketing service by Panasonic (Japan) [9].

Although OCC does not support high-capacity transmission links, which is due to the speed limit of cameras, it can be employed in numerous low R_b and short-range indoor and outdoor IoT applications, including device-to-device communications, indoor positioning, localization, navigation, intelligent transportation systems, financial transactions, motion-based device control, small identification information, and communications through advertisements [3,10,11]. Note that in IoT-based smart environments links with R_b of a few kb/s are sufficient for information transmission and therefore there is no need for medium-speed transmission capabilities. However, the major challenge in implementing systems with a low R_b is the requirement for flicker-free transmission. Authors established flicker-free communications links using the grouped LED array concept in [12] using RS-based capturing Rx with a R_b of ~ 1 kb/s. The RS acquisition mechanism that sequentially integrates light on rows of pixels is the major advantage of CMOS IS used as the Rx in OCC [13].

In OCC, the transmitted light signal will arrive at the Rx (i.e., IS) via both the line-of-sight (LOS) and non-LOS (NLOS) paths. However, the LOS becomes the dominant path when using Tx's and Rx's with very narrow fields of view. The RS-based MIMO–OCC transmission links are:

- a. *LOS MIMO–OCC links.* Traditional indoor VLC or LOS OCC links with a high R_b over a range of transmission spans have been adopted in many applications, including: (i) short-range RS-based indoor MIMO–OCC LOS (1–5 m) flicker-free links using multilevel intensity modulation (IM) with a R_b of 10 kb/s [14]; (ii) a beacon jointed packet reconstruction scheme with a R_b of 5.76 kb/s [15]; (iii) screen modulation techniques followed by the $2M$ -ary quadrature amplitude modulation format [16]; (iv) a CMOS RS effect-based scheme using the grayscale value distribution and machine learning algorithm to enhance R_b [17]; and (v) the raptor code with linear time encoding and decoding with a R_b of 1 kb/s [18]. Note that in LOS-based systems it is possible that some NLOS may be detected at the Rx, which will result in a time delay spread.
- b. *NLOS MIMO–OCC links.* In scenarios such as device-to-device communications, it is possible that there might not be a LOS path between the Tx's and the Rx's. Therefore, the communications will be via the NLOS paths, which offer mobility and flexibility but at the cost of a lower R_b [19,20]. NLOS–MIMO links based on space and the time division multiple access technique with a R_b of ~ 1 kb/s and flicker-free transmission over a 10 m link span was reported in [19]. A 152 bits NLOS link (1.5 m) with a low level of error correction code using image processing techniques such as background compensation blooming mitigation, extinction-ratio enhancement, and Bradley adaptive thresholding for RS demodulation was investigated in [21].

- c. *Tx and Rx orientations.* Unlike previous studies, which focused on either a LOS or NLOS link, in MIMO–OCC links we need to consider both the Tx and Rx orientation angles. Some practical solutions considering different orientations and placements of the Tx and the Rx to support mobility scenarios in an indoor environment must be focused. In [6], the angular rotation θ from 0° to 70° along with parallel movement of a red, green, and blue based (RGB-based) LED array (16×16 LEDs) Tx and a 330 fps camera-based Rx operating in the GS capturing mode over a link span of 60 cm was reported. Note that in [6], the refresh rate for the LED array was set to 82 Hz, which is less than the MFTP standard rate of 200 Hz [4], thus providing flickering transmission and rotation support over a link span of 60 cm [6]. On the other hand, a 60-LED-based array is used to provide both data transmission and frame synchronization. In [22], a practical orientation independent RS-based NOLS–OCC link performing wide Rx's orientation for indoor applications with a R_b of ~ 7 kb/s over a transmission link span of 50 cm was presented. However, the Tx should be designed in such a way to ensure that there are sufficient reflections from many directions to ensure link availability. In [23], a CMOS RS pattern decoding scheme using the grayscale redistribution and differential grayscale packet selection was proposed and investigated to improve the decoding performance of the links under translational or rotational motions. The authors showed no significant signal degradation over a transmission range of up to 150 cm. Note, in applications with mobility, to ensure link availability, it is necessary to investigate various transmission scenarios considering different Tx's angular orientations heights and distances from each other as well as from the Rx.

In this paper, we study multichannel MIMO–OCC considering the angular rotation of the Tx's located at the same distance but different heights and distances from each other. These transmission setups are defined considering the indoor dynamic, mobility, and multicasting scenarios in places such as shopping malls, hospitals, and offices, where the number of Tx's can be placed at different locations with different angles depending on the interior design and the illumination requirements. The proposed scheme offers a valid solution irrespective of the availability of LOS and NLOS paths. It is based on the optimum angular orientation of multiple Tx units for practical indoor IoT-based scenarios such as mobility and multi-Tx/Rx (multiuser). The proposed scheme employs two MIMO–OCC Tx units with a simplified design and a commercial low-cost Raspberry Pi camera (RaspiCam) as the Rx. The lab-scale experiments are carried out for two different transmission setups, where the effect of the optimum angular orientation θ of two Tx units located at different heights and distances from each other, as well as the camera-based Rx, is analyzed. For this reason, the spatial frequency f_{sf} which represents the projection of a target, i.e., the Tx LED array over a captured image in terms of pixels, is used. The quality matrices of the captured image in terms of the peak signal-to-noise (PSNR) and the success rate of received bit sequences for a range of θ with respect to the f_{sf} , L , and SS are also analyzed.

This paper has five sections. Section 2 describes the proposed MIMO–OCC system, Section 3 shows the measurement setup followed by the experiment results and analysis in Section 4. Conclusions are then drawn in Section 5.

2. PROPOSED MIMO–OCC SYSTEM

A. CMOS IS Noise Characterization Within MIMO–OCC

The block diagram of the proposed MIMO–OCC system with multiple Tx_s (Tx₁–Tx_{*n*}) and IS Rx is shown in Fig. 1(a). At the Tx, the data is generated in the form of on-off keying nonreturn to zero (OOK–NRZ) format $s(t)$ and is used for the IM of the LED via the LED driver. At the Rx, using an optical lens the IS captures multiple light Tx_s as different point sources on different sections of the IS. It is therefore straightforward to separate the multiple captured point sources and apply image processing for data detection. In this work, for further analysis we consider the projection of one Tx on to the Rx (i.e., camera), which can also be applied to multiple captured point sources. The intensity-modulated light signal $x(t)$ is transmitted over a free space channel and is captured at the Rx using a CMOS RS-based camera. For the LOS link, the received signal is given by [24]

$$y(t) = \eta x(t) \otimes h(t) + n(t), \tag{1}$$

where $h(t)$ is the combined impulse response of the channel and camera, η is the quantum efficiency of the IS, \otimes is the time domain convolution, and $n(t)$ is the additive white Gaussian noise including the ambient light induced shot noise and the noise in the camera (i.e., fixed pattern, thermal (FPN)), photocurrent shot (optical excess and electronics), and flicker noise sources), as shown in Fig. 1(b) [25]. If the definition of power is scaled by the number of points in the signal, it will give the mean squared error (MSE). This notion can be extended in OCC for actual transmitted and received images by summing up twice the rows and columns of image vectors or stretching the entire image into a single vector of pixels and applying the one-dimensional

(1D) definition. Therefore, in OCC signal images the SNR can be given as

$$\text{SNR (dB)} = 10 \log_{10} \frac{\sum_{m=1}^W \sum_{n=1}^H I_{Tx}(m, n)^2}{\sum_{m=1}^W \sum_{n=1}^H [I_{Tx}(m, n) - I_{Rx}(m, n)]^2}, \tag{2}$$

where $I_{Tx}(m, n)$ and $I_{Rx}(m, n)$ denote the intensity of the pixel of the transmitted and received image frames, respectively, at the location (m, n) . In Eq. (2), $[I_{Tx}(m, n) - I_{Rx}(m, n)]^2$ corresponds to the squared error between the original and corrupted signals as $|y(t) - x(t)|^2$. The size of the image is W (width) \times H (height). High values of SNR show that the estimation error is small and, therefore, among various image fusion methods the ones that exhibit higher SNR values can be considered to improve performance. The PSNR and the MSE are measured similarly to the SNR, which are defined as [26,27]

$$\text{PSNR (dB)} = 10 \log_{10} \frac{I_{\text{peak}}^2}{\text{MSE}}, \tag{3}$$

$$\text{MSE} = \frac{\sum_{m=1}^W \sum_{n=1}^H [I_{Tx}(m, n) - I_{Rx}(m, n)]^2}{N_{\text{column}} \times N_{\text{row}}}, \tag{4}$$

where I_{peak}^2 denotes the squared peak intensity of the measured frame, and N_{column} and N_{row} are the number of columns and rows of the images, respectively. It can be seen that $\text{PSNR} \geq \text{SNR}$. Both will be equal only when the original clean signal is constant and with the maximum amplitude. In the case of PSNR, the major focus is on the peak intensity I_{peak} of the measured frame to determine the signal bandwidth or number of bits to represent the signal. Therefore, the major issue is how the high-intensity regions of the image will be affected by the noise. This is much more content-specific than the SNR, which can be adopted in many applications, such as image compression.

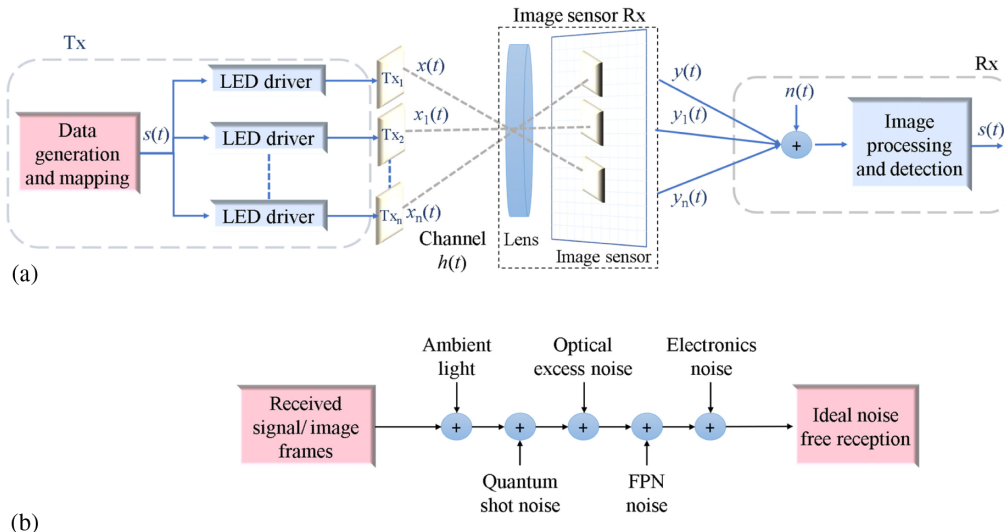


Fig. 1. (a) Schematic block diagram of MIMO–OCC link. (b) Different sources of noise in the OCC Rx end.

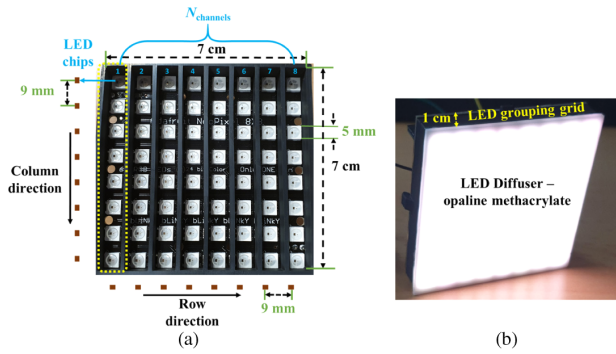


Fig. 2. Tx configuration: (a) Tx dimensions with LED grouping and (b) Tx with LED grouping grid and diffuser.

B. Developed MIMO-OCC System

A simple design of the MIMO Tx unit is adopted from our previous work in [12], as illustrated in Fig. 2. It is composed of a 64-NeoPixel array with an 8×8 small-chip LED [28], as shown in Fig. 2(a), and a 1 cm thick LED grouping grid that is placed over the Tx LED array, as shown in Fig. 2(b). The LED grid is designed to divide a 64-NeoPixel chip LED into eight different column-wise groups with eight chip LEDs per group to allow eight different data transmission channels using a single NeoPixel LED array. A 2 mm thick opaline methacrylate LED diffuser, which is commonly used, is placed over the Tx. The size of the LED array is $7.2 \times 7.2 \text{ cm}^2$. The characterization of the proposed MIMO Tx unit in terms of its optical radiation pattern and output optical power-current-voltage ($L_{\text{lux}}-I-V$) curves was performed in [12]. Note, it is recommended to drive each LED with $I_{\text{LED}} = 20 \text{ mA}$ [12,28]. Therefore, for the LED array, the drive current $I_{\text{LED-array}}$ was set to 1.28 A to measure $L_{\text{lux}}-I-V$. It was found that the NeoPixels used either as a single LED chip or an LED-array together with the grid and diffuser depicted linear $L_{\text{lux}}-I-V$ plots, which are highly desirable in IM VLC systems [12].

Figure 3 illustrates the data mapping on the controller side for the proposed MIMO-OCC using two 64-NeoPixel Tx units and an Arduino Uno microcontroller-based driver per Tx. NeoPixels are controlled using Arduino software. First, N_{pixels} are assigned to N_{chips} per NeoPixel Tx, which are then grouped, column-wise, into $8-N_{\text{channels}}$. To support rotational movements and study the angular behavior of multichannel Tx, the rotation angle within the range of $0^\circ < \theta < 90^\circ$ was changed at 10° steps, as shown in the inset (i) of Fig. 3. The data generated using the Arduino unit is mapped to the LED addresses with a frequency $f_s = (t_{\text{chip}})^{-1}$, where t_{chip} is the 1-bit time per NeoPixel

chip with the minimum value set to 2.5 ms due to a Arduino hardware limitation to ensure flicker-free transmission at a f_s of 400 Hz [12]. NRZ-OOK data bit streams with RGB (P_i , P_j , and P_k) as $P_i + P_j + P_k = 1$ and $P_i + P_j + P_k = 0$ is used for the IM of Tx for transmission over the free-space channel. Note, the same data is transmitted by all eight LEDs per N_{channel} , as shown in Fig. 4, while Tx 1 and 2 are transmitting different data signals. For example, the predefined 8-bit data in $N_{\text{channel}1}$ shown in Fig. 4(a) is transmitted by all eight LEDs in the Tx₁, as shown in Fig. 2(a). Note that the data is transmitted simultaneously by all the channels in Tx₁ and Tx₂. Moreover, the $N_{\text{channel}1}$ is the inverted version of $N_{\text{channel}2}$ in the Tx₁, which is adopted for the synchronization of each LED group transmitting different packets. The anchor-based transmission needs considering when (i) transmitting long data streams via the proposed Tx design or in other techniques such as massive MIMO [6]; and (ii) for links experiencing blocking and shadowing [11].

Figure 5 shows an example of the RS-based capturing of the proposed multichannel Tx. In the RS-based capturing mode, the camera sequentially integrates all illuminated pixels at the exposure time $t_{\text{two-exp}}$, which is the same as scanning. The RS-based Rx reported in the literature captures a single bit for $t_{\text{two-exp}}$ [16]. In RS-based cameras, the readout time t_{readout} ensures that there is no overlapping of the rows of pixels and allows multiple exposures of a single captured image. In the proposed scheme, using multichannel Tx, 8 bit (1 bit per channel) of data are captured in a single row over $t_{\text{two-exp}}$, as shown in Fig. 5. This approach ensures flicker-free transmission at a higher R_b , in contrast to traditional RS schemes capturing only a single bit/ $t_{\text{two-exp}}$. Note that the proposed Tx has a small surface area for capturing sufficient lights with a controller limitation defined by a f_s of 400 Hz. In flicker-free transmission, the R_b can be improved by increasing the surface area of the Tx unit (i.e., a higher number of LEDs).

The number of rows depends on the R_b and the transmission distance. The maximum number of visible bits per group in a single frame and the frame time are given as

$$N_{\text{visible}} = \lfloor t_{\text{frame}} \cdot f_s \rfloor. \quad (5)$$

$$t_{\text{frame}} \leq N_{\text{row}} \times t_{\text{row-shift}} + t_{\text{row-exp}}, \quad (6)$$

where N_{row} is the pixel rows, which is based on the camera resolution; $t_{\text{row-shift}}$ is the row shift; and t_{frame} is frame time. Note that: (i) $t_{\text{row-exp}}$ of the last row per frame is a very small value; and (ii) in the RS-based capturing mode, there is a delay in the start of each row, which results in a $t_{\text{row-shift}}$. It was shown in [12] that

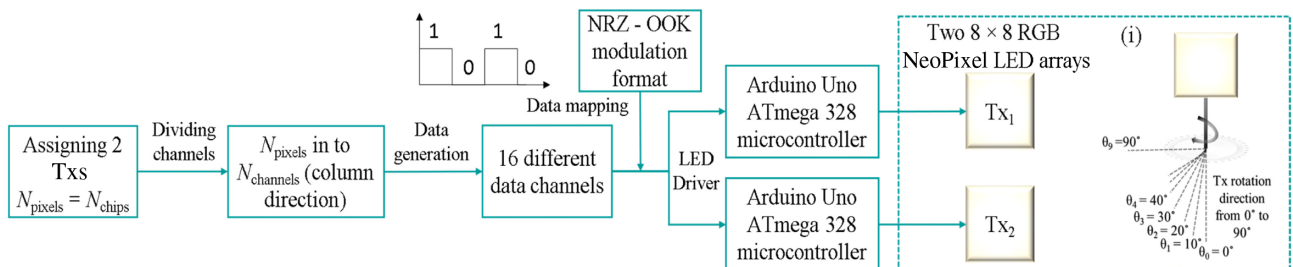


Fig. 3. Data mapping in Arduino domain: inset i) angular orientation of Tx.

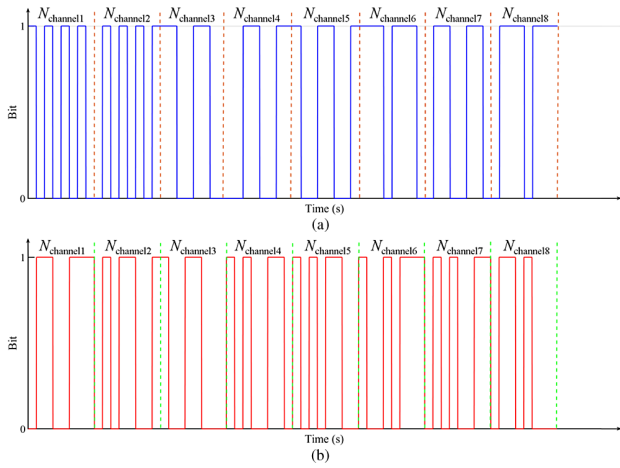


Fig. 4. Transmitted bits through (a) Tx₁ and (b) Tx₂.

N_{visible} will change with respect to both the distance between the Tx and the Rx and the camera resolution. Based on N_{visible} , the data transmission rate is given as

$$R_b = N_{\text{channels}} \times f_s, \quad (7)$$

where N_{channels} is the number of LED groups in the Tx unit.

C. Detection Scheme to Study the Tx Angular Rotation Influence

Figure 6 illustrates the flowchart for the detection when considering the Tx's angular rotation as $0^\circ < \theta < 90^\circ$ in the proposed

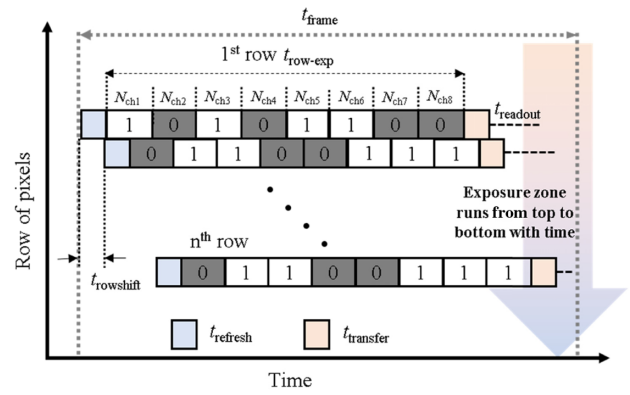


Fig. 5. RS-based capturing of the proposed multichannel Tx.

systems. At the Rx, we used a Raspicam with a given SS, resolution, and frame rate for capturing images (i.e., recording a video stream for 5 s) of IM light sources over L of 30 to 110 cm. The overall detection process is divided into three main stages: *Stage 1: Video recording and frame division.* The Raspicam Rx records the data and calibration video streams that represent the captured transmitted information and the Tx's template shape, respectively. The calibration videos, which outline the intensity compensation of the data video frames, are used for equalization as the IS captures multiple light Tx's as different point sources on different sections of the IS. Therefore, the image frame is divided to distinguish multiple light sources for detection. Note that a considerably smaller image containing the signal information is transmitted to reduce the processing time at the Rx.

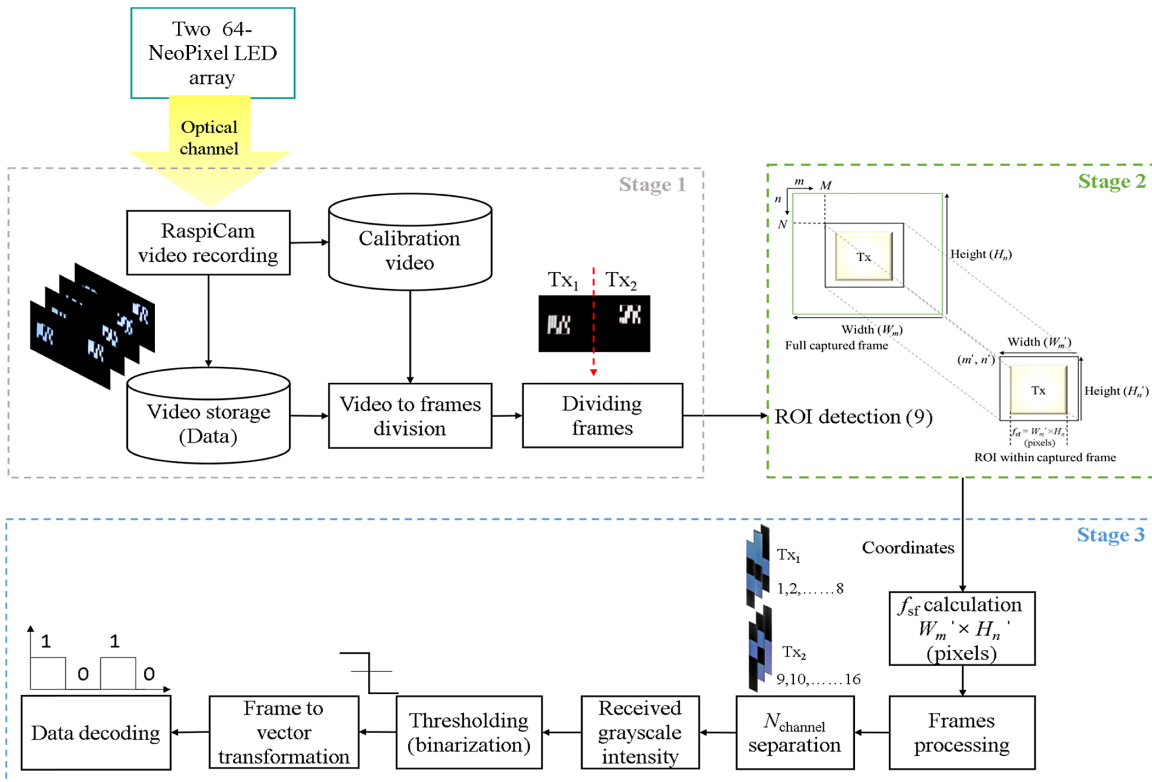


Fig. 6. Flowchart illustrating the data detection process.

Stage 2: Region of interest (ROI) detection. Here, we perform ROI detection [29] over the divided frames, and then use the obtained coordinates, which define boundaries of the ROI, for image cropping. The ROI template used to define ROI in the full calibration capture frame. It is given as

$$\text{ROI} = (m', n', W'_m, H'_n), \quad (8)$$

where m' and n' are top corner coordinates, and W'_m and H'_n are the width and height of the captured image frame, respectively. Here, we have adopted an image processing technique known as template matching [30] to determine the target ROI in the calibration image frame and then to find the position of the target ROI_{temp} in the data image frame, given as [30]

$$\text{ROI}_{\text{temp}} = \sum_{m=0}^{W_m} \sum_{n=0}^{H_n} \{P(m', n') - P'(M + m', N + n')\}^2, \quad (9)$$

where the coordinate of a single point in ROI is (m', n') with a pixel value $P(m', n')$, while the coordinate of the overlapping point and its pixel value are $(M + m', N + n')$ and $P'(M + m', N + n')$, respectively. The overlapping points of the data image frame and ROI image are calculated using template matching. The coordinate (M, N) is the origin of the template image on the full captured image. It is assumed that the sizes of the template and the fully captured input image are $W'_m \times H'_n$ (width \times height) and $W_m \times H_n$ (width \times height), respectively. The ROI_{temp} obtained from Eq. (9) is used to crop the data image frames. The values of ROI_{temp} must change dynamically because in this technique the shape of the Tx unit changes with θ and the distance between the Tx and the camera settings. This technique can be further adapted to detect multiple ROIs within a single image frame based on its template coordinate points.

Stage 3: Frame processing and data detection. The ROI cropped images from the previous stage are used to calculate the spatial frequency components f_{sf} , which refers to the projection of a target (i.e., the Tx LED array over a captured image in terms of pixels [30, 31]). As shown in Stage 3 of Fig. 6, in terms of pixels f_{sf} of ROI_{temp} is $W'_m \times H'_n$. Next, f_{sf} separated images are processed for N_{channel} separation followed by image processing. As outlined in Stage 3 of Fig. 6, each N_{channel} is converted from the RGB color format to the grayscale for both calibration and data frames to retrieve the intensity profile. As the intensity levels for NRZ-OOK data signals are set as $P_i + P_j + P_k = 1$ (with $I_{\text{peak}} = 255$) and $P_i + P_j + P_k = 0$, the threshold level is set based on the average of the received image intensity profile in ROI. Following thresholding, binarization of the data frames is performed to convert the frame into a vector transformation, which is applied to the remaining frames for decoding the transmitted data bit streams. Finally, the received data bit vector is then compared with the transmitted data to ascertain the success of the reception of received bits by determining the ratio of the wrongly decoded bits to the total number of transmitted bits (i.e., the number of bit errors).

3. MEASUREMENT SETUP

The measurements were performed for two different transmission setups, as illustrated in Fig. 7. As previously mentioned, this investigation focused on the angular rotation of Tx units within multichannel OCC. Both Tx units rotate with θ of 0° to 90° . A Raspberry Pi camera used as a Rx is mounted at the top of the display panel at a height h_{Rx} of 18 cm and an angle θ_c of 90° , as shown in Fig. 7. In both the setups, the radial distance r between the Tx_1 and Tx_2 is changed with respect to the transmission length L between camera and the Tx's. Note, r was increased to ensure that both Tx units are captured at the same time in a single image frame.

In transmission setup 1, both Tx units are placed at the same distance but different heights h_{Tx_1} (same as the camera height h_{Rx}) and h_{Tx_2} at 25 cm, as shown in Fig. 7(a). Note that the actual transmission distance between both Tx units and camera is $l = \sqrt{L^2 + (\frac{r}{2})^2}$, as shown in Fig. 7(a). For example, for L and r of 30 and 20 cm, l is ~ 32 cm. Note that the difference between L and l is rather small; therefore, for further analysis and simplicity we will only use L .

In transmission setup 2, both Tx units are placed at the same height $h_{\text{Tx}} = h_{\text{Rx}}$, but at different distances L_1 and L from the camera, as shown in Fig. 7(b), where $(L_1 - L) = 30$ cm.

The experimental setups to investigate the angular behavior of the proposed MIMO-OCC scheme are shown in Fig. 8.

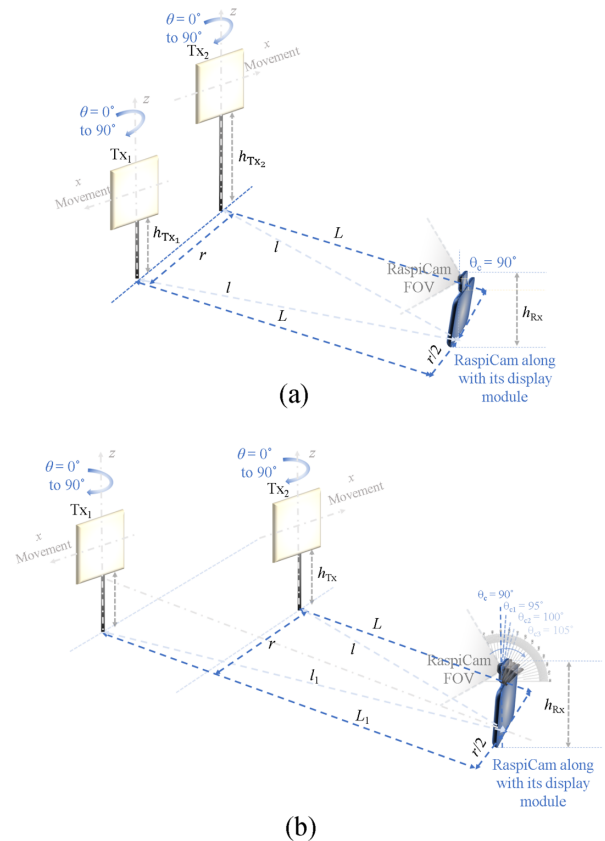


Fig. 7. Transmission setups: (a) Tx units placed at different heights and (b) Tx units placed at a different distance.

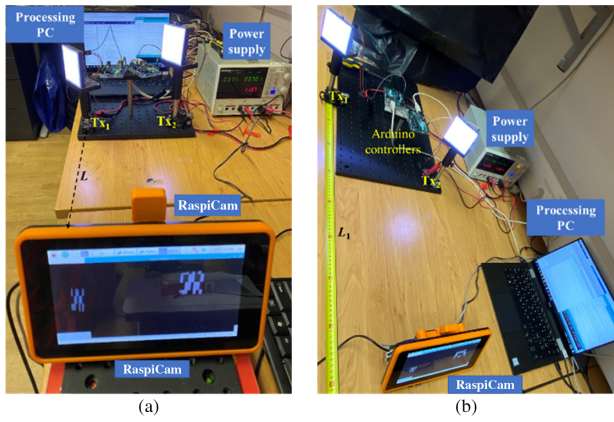


Fig. 8. Experiment setup: (a) Tx units placed at different heights and (b) Tx units placed at a different distance.

Table 1. Key Parameters of the Experimental Setup

Parameter	Value
RaspiCam chip size	5.09 mm (H) × 4.930 mm (W) Diagonal: 4.60 mm
RaspiCam resolution	1920 × 1080 pixels
Raspberry display size	7" (diagonally)
Raspberry display resolution	800 × 400 pixels
t_{chip}	2.5 ms
f_s	400 Hz
RaspiCam frame rate	30 fps
N_{row}	1080 pixels
Tx	8 × 8 RGB NeoPixel LED array
N_{channels}	16 LED groups with eight groups each Tx and 8LED/group
$I_{\text{LED-array}}$	1.28 A (for each Tx unit)
t_{frame}	0.216 ms
SS	200, 400 and 800 μs
R_b	6.4 kbps
L	30–110 cm
L_1	60–140 cm
r	25–45 cm
Tx Rotation angle θ	0°–90°
Rx angle θ_c	90°

The Tx units are controlled using an Arduino Uno board, which is an open source microcontroller board based on ATmega328 [32]. A 64-bit long data stream (i.e., eight bits per group, as shown in Fig. 4) is generated in the Arduino software domain for each Tx unit and mapped to each LED (i.e., address) using the Arduino Uno board. The key experimental parameters are listed in Table 1. A Raspberry Pi (PiCamera V2) is the camera used, which is based on a Sony IMX219 sensor [33]. The RaspiCam is attached to the Raspberry touchscreen display to provide easy interface and control over the camera capturing modes and settings. Experiments were performed for nine transmission distances and three different values of SS (see Table 1) for θ of 0° to 90°. The NRZ–OOK signal was recorded for 5 s (a total of 150 frames).

4. EXPERIMENTAL RESULTS AND ANALYSIS

A. Tx Units Placed at the Same Distance and Different Heights

Figure 9(a)–9(c) show examples of captured image frames, f_{sf} and the grayscale intensity profiles for the detected data per N_{channels} for a range of L , θ , and SS. It can be seen that the shape of the captured Tx changes due to angular tilting, which results in the loss of data bits. To avoid this, the first and last pixel rows in each image frame are eliminated from the top and bottom of each Tx ROI. The received intensity distribution within the image frame is shown in the form of grayscale intensity profiles for the captured original images. These intensity profiles play an important role in determining the higher and lower intensities (i.e., representing 1 and 0) in the received image frames for further thresholding and demodulation [11]. The dotted yellow box in the original image frames defines the ROI, which fills only the f_{sf} of the captured Tx within the full image frame. The clear and sharp distinction between the data lines can be seen for θ up to 40°, and L and SS of 50 cm and 200 μs , respectively, as shown in Fig. 9(a). Since the lines get saturated for higher values of θ , which reduces the f_{sf} and SS, as shown in Figs. 9(b) and 9(c), it makes it challenging to separate N_{channels} , which then affects the data demodulation (i.e., higher number of error bits). We have therefore shown the intensity distribution in the form of a quantized intensity profile of the captured image frame for θ of 70°, L of 90 cm, and SS of 800 μs , [Fig. 9(c)]. Therefore, data detection at L up to 110 cm was performed for θ up to 80° with SS of 200 and 400 μs , and θ of 70° with SS of 800 μs .

Table 2 shows the average f_{sf} of the captured Tx image with respect to L and θ . It can be seen that the f_{sf} (reduces) and the shape (square to rectangle) of the Tx changes with L and θ . Considering the average f_{sf} , we see very little changes in L (10 cm) and θ (10°). For a L of 30–50 cm, the f_{sf} has ~2 and 3 times more high-frequency components than for a L of 60–90 cm for a range of θ , [Figs. 9(a)–9(c)]. Therefore, it can be said that a reduced number of pixels of the Tx image leads to lower high-frequency components and, consequently, the channel can be seen as a low-pass filter with a cutoff frequency that decreases with increasing L and θ . Further analysis is performed for f_{sf} at different values of L and θ and its impact on the communications link performance in terms of successful reception and PSNR.

Figure 10(a) then illustrates the performance analysis of the angular behavior of the multichannel MIMO–OCC link in terms of the percentage success of the received bits with respect to θ for various values of L and SS. In this setup, the average time window for offline OCC data extraction (only) was about 0.98 s using the predefined data processing algorithm depicted in Fig. 6. It can be seen that, for L up to 80 cm, 100% reception success is achieved for θ of 50° for SS of 200 and 400 μs ; and for θ of 30° for SS values of 800 μs , [Fig. 10(a)]. Note that, for L of 30 cm, 100% success is achieved for θ of 0° to 80° and for SS values of 200 and 400 μs . It can also be seen that the reception success reduces further with f_{sf} (i.e., less than ~50% at θ of 0°, as shown in Table 2), and increases with SS, which results in channel saturation. As a result, it is challenging to separate the N_{channels} and, therefore, the decoding of received bits, [Figs. 10(a)].

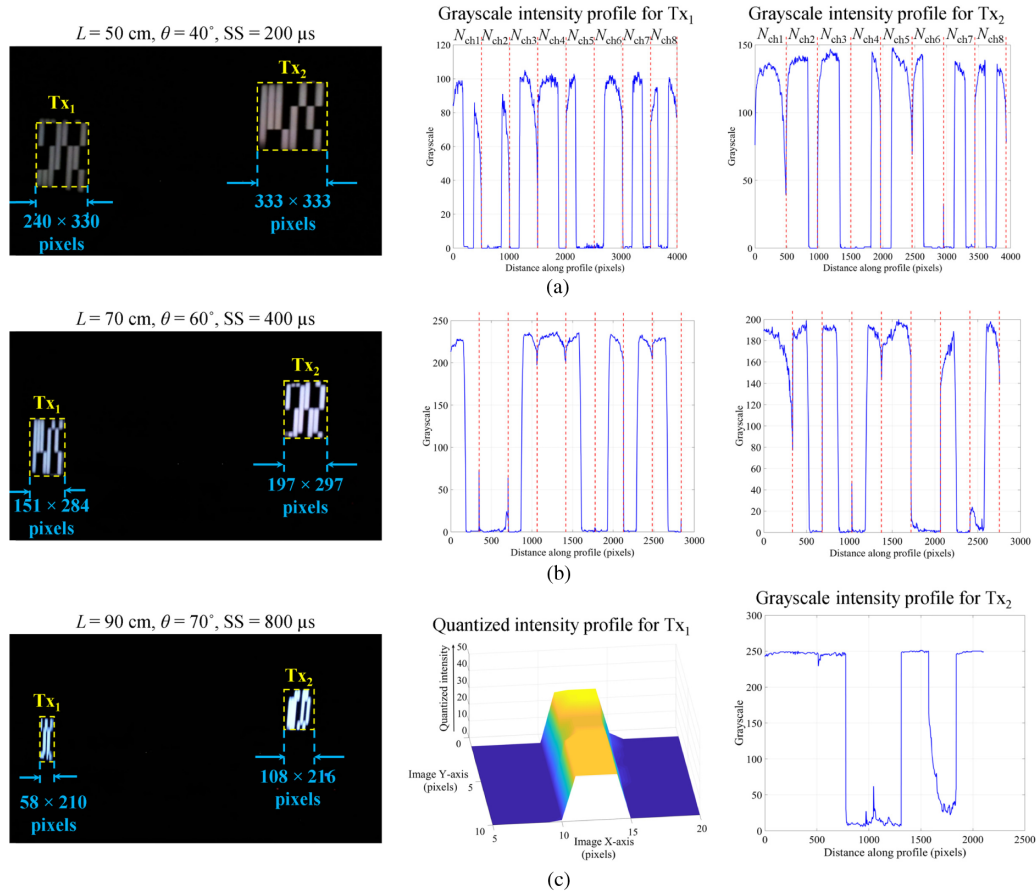


Fig. 9. Grayscale and quantized intensity profiles of originally captured images for data detection at: (a) L of 50 cm, θ of 40° , and SS of $200 \mu\text{m}$, (b) L of 70 cm, θ of 60° , and SS of $400 \mu\text{m}$, and (c) L of 90 cm, θ of 70° , and SS of $800 \mu\text{m}$.

Table 2. Average f_{sf} in Pixels with Respect to L and θ^a

L (cm)	θ 0° – 20°	θ 30° – 50°	θ 60° – 80°
30–50	450×450	210×310	200×300
60–80	459×459	300×300	171×290
90–110	155×285	150×280	145×260
	200×299	195×294	185×285
	78×230	65×215	55×200
	115×240	105×235	100×125

^aUpper values are for the Tx_1 and bottom for the Tx_2 .

As previously mentioned in Section 2, in OCC, the data is captured in the form of a 2D image; therefore, the conventional SNR measurement cannot fully reflect the quality of the link. Here, we have adopted PSNR, which is widely used as a quality metric in image processing systems. Equations (3) and (4) are used to compute the MSE between the transmitted and received images with respect to ROI_{temp} [Eq. (9)] as given by

$$\text{MSE} = \frac{\sum_{m=1}^{W_m} \sum_{n=1}^{H_n} [ROI_{\text{temp}}(m, n) - I_{\text{RX}}(m, n)]^2}{W_m \times H_n}. \quad (10)$$

As the input image has an 8-bit unsigned integer data type with $I_{\text{peak}}^2 = 255$, the PSNR is computed by substituting

Eq. (10) and I_{peak}^2 in Eq. (3). Figure 10(b) shows the performance of the OCC link in terms of PSNR with respect to θ for different values of SS and link spans. As shown, PSNR increases with SS due to the fact that the images of captured Tx at higher SS are more saturated compared to those captured at a lower SS, as shown in Fig. 9(c). Note that the PSNR decreases with a decreasing f_{sf} [70% than at θ of 0° , as shown in Table 2 and Fig. 10(b)] with respect to θ and L . This is due to the fact that the Tx units move away from the camera field of view with increasing θ and L ; therefore, a small amount of light passes through the camera lens and hence fewer photons are incident on the pixels of the image sensor and thus, there is reduced f_{sf} . With 100% reception success, the PSNR value of ~ 22 dB is measured for SS of $200 \mu\text{m}$, which increases by 3 and 7 dB for SS of 400 and $800 \mu\text{m}$, respectively, for L of 30 cm at θ of 0° .

Based on the N_{channel} and N_{visible} for each Tx unit in the image frames, the data throughput is given as

$$\text{Data throughput} = N_{\text{channel}} \times N_{\text{visible}} \times \left(\frac{\text{fps}}{2} \right). \quad (11)$$

Figure 11 illustrates the performance analysis of the proposed multichannel MIMO–OCC in terms of data throughput calculated with respect to θ and L . For θ of 0° , the maximum data throughput of 1.92 kb/ps is observed for a L of 30 cm, where an 8-bit data stream (4-bit/ N_{channel} /Tx) is seen by the

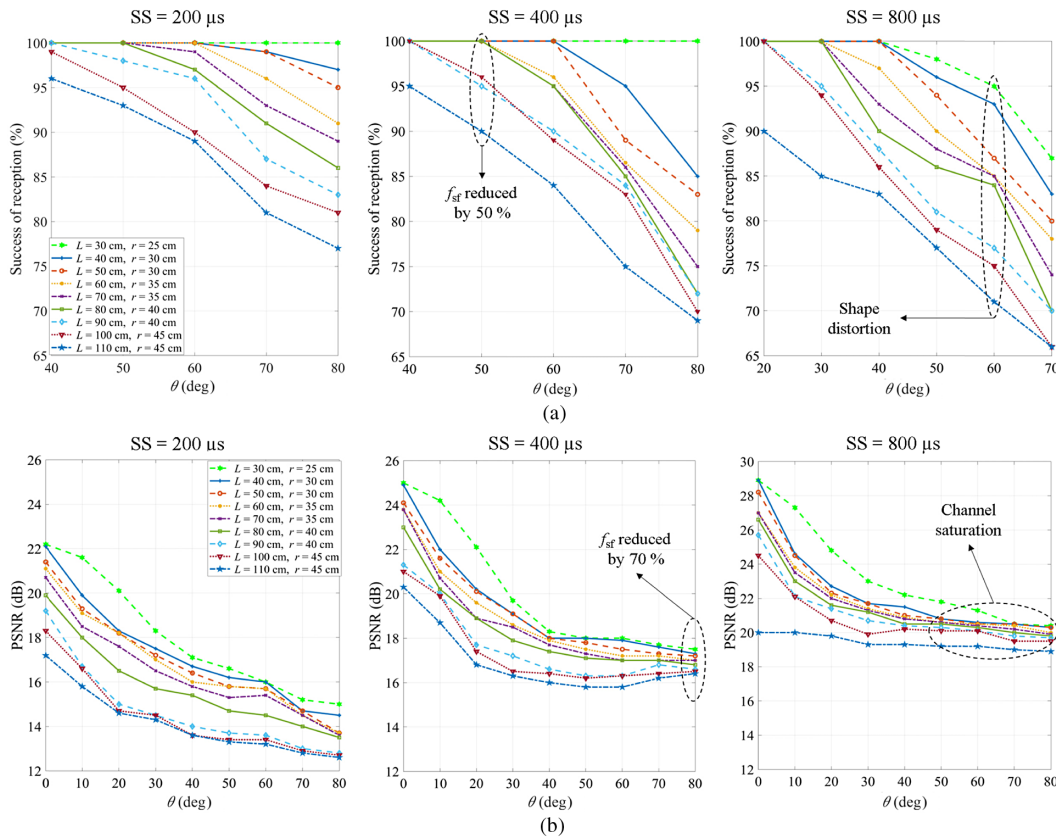


Fig. 10. Performance analysis: (a) success of reception and (b) PSNR.

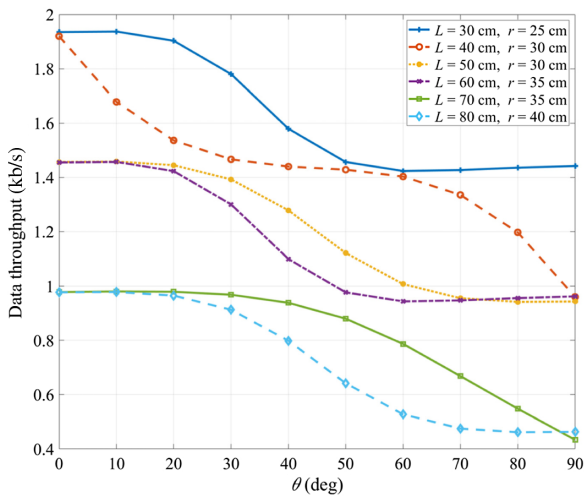


Fig. 11. Data throughput with respect to change in L and θ .

camera. The f_{sf} is decreased with increasing L and θ , thus resulting in a reduced N_{visible} and data throughput. For θ of 40°, the data throughput of 1.44 kb/s is observed for a L of 50 cm, where a 6-bit data stream (3-bit/ N_{channel} /Tx) is seen by the camera, as shown in Fig. 9(a). For a L of 90 to 110 cm, a 2-bit stream (1-bit/ N_{channel} /Tx) is visible to the camera, as shown in Fig. 9(c), and therefore the data throughput of 480 b/s is obtained for each θ .

B. Tx Units Placed at Different Distances

Figure 12 shows the captured image frames, f_{sf} and the grayscale intensity profiles of the detected data for each N_{channels} , L , θ , and SS. The clear and sharp distinction between the data lines can be seen at θ of 20° and 30°, L of 40 and 60 cm, and SS of 200 and 400 μ s, respectively [Fig. 12(a)]. Note that in this setup, due to an increasing tilting angle θ , the Tx₁ at L_1 of 130 cm is not visible and the Tx₂ at L of 100 cm is too small to separate the N_{channel} for demodulation, as shown in Fig. 12(c). Therefore, data detection was carried out for L up to 90 cm at θ up to 70° for all values of SS.

Table 3 shows the average f_{sf} of the captured Tx image with respect to L and θ . The f_{sf} for the Tx₂ (closer to the Rx) at L of 30–40 cm has ~ 2 to 3 times more high-frequency components than the Tx₁ (closer to the Rx) for L of 60–70 cm with respect to θ , as shown in Figs. 9(a)–9(c). In this case, it can be said that the large reduction in the f_{sf} of the Tx image is due to r between the Tx's. An increase in r and θ reduces the f_{sf} , which results in higher bit errors and a lower PSNR.

Figures 13(a) and 13(b) illustrate the performance analysis of the angular behavior of the multichannel MIMO–OCC link in terms of the percentage of the success of the received bits and PSNR. In this setup, the average time window for offline OCC data extraction (only) was about 1 s using a predefined data processing algorithm, as shown in Fig. 6. It can be seen that for L and L_1 of up to 60 and 90 cm, a 100% success is achieved for θ of 40° with SS of 200 and 400 μ s and for θ of 30° with SS of 800 μ s, as shown in Fig. 13(a). As previously mentioned, the

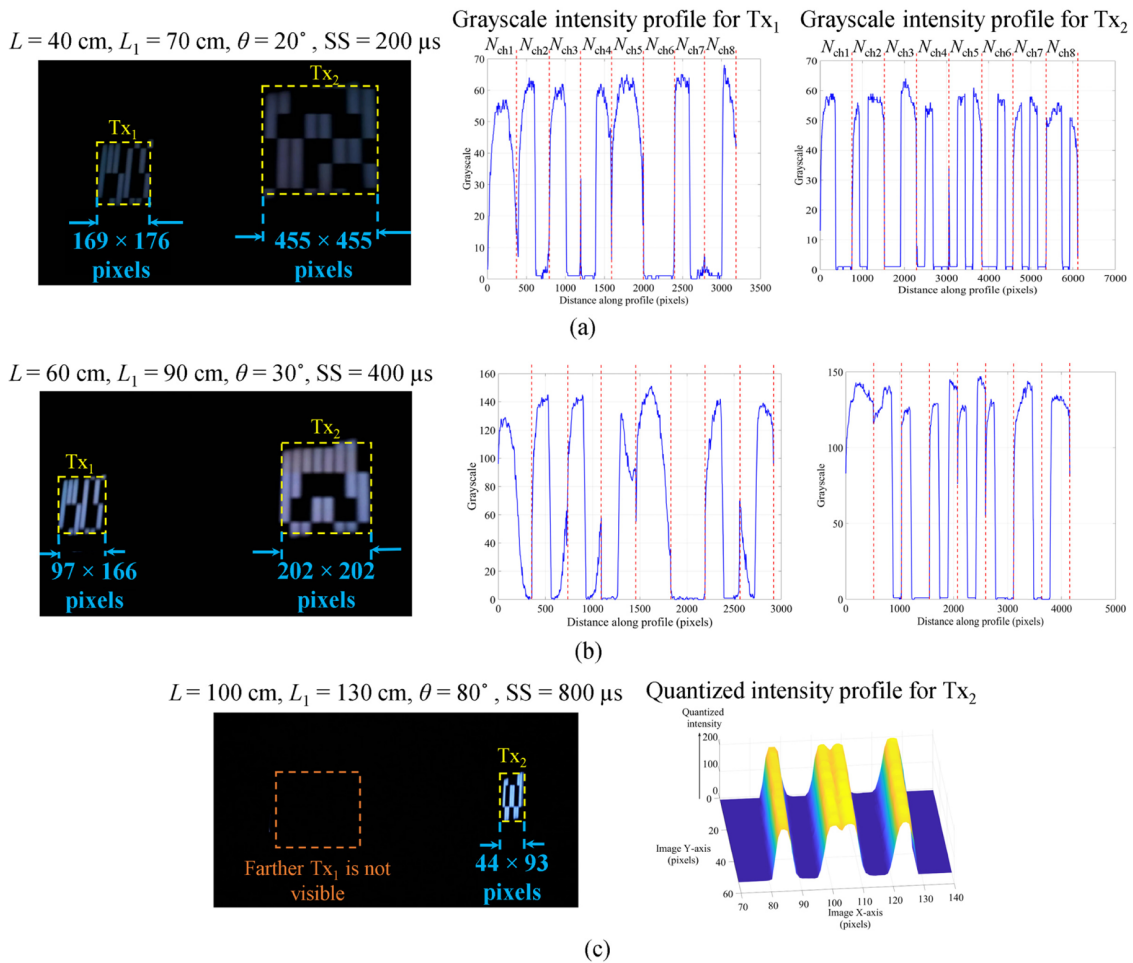


Fig. 12. Grayscale and quantized intensity profiles of originally captured images for data detection at: (a) L of 40 cm, θ of 20° , and SS of 200 μs , (b) L of 60 cm, θ of 30° , and SS of 400 μs , and (c) L of 100 cm, θ of 80° , and SS of 800 μs .

Table 3. Average f_{sf} in Pixels with Respect to Ranges of L and θ (Upper values are for the Tx_1 and bottom for the Tx_2)

L and L_1 (cm)	θ 0° – 20°	θ 30° – 50°	θ 60° – 70°
60–70	165 × 175	160 × 210	148 × 200
30–40	450 × 451	349 × 351	170 × 289
80–90	210 × 210	190 × 200	125 × 155
50–60	100 × 170	95 × 165	80 × 150
90	100 × 160	70 × 150	56 × 175
120	80 × 155	50 × 140	40 × 100

data reception success is also affected by the f_{sf} . Note that in this setup the Tx_1 is placed farther than the Tx_2 with respect to the camera. Therefore, with an increasing L and θ , the f_{sf} becomes smaller [f_{sf} is reduced by 80% for θ increasing from 0° to 70° for all values of L , as shown in Table 3 and Fig. 13(b)]. Note that at $L = 100 \text{ cm}$ and $L_1 = 130 \text{ cm}$, the Tx_1 is no longer seen by the camera, as shown in Fig. 12(c). The PSNR of $\sim 13 \text{ dB}$ is measured for a SS of 200 μs , which is increased by 2 and 6 dB for a SS of 400 and 800 μs , as shown in Fig. 13(b), respectively, for L of 90 cm at θ of 70° . The maximum PSNR of 22, 25, and

29 dB are observed for a SS of 200, 400, and 800 μs , respectively, for a L of 30 cm and θ of 0° .

Figure 14 illustrates the data throughput as a function of θ for the proposed multichannel MIMO–OCC system. The data throughput decreases with the f_{sf} due to the increased link span and θ . For θ of 0° , the maximum data throughput of 1.68 kb/s is observed at L of 40 cm, where the 7-bit data stream (3-bit/ N_{channel} for Tx_1 and 4-bit for Tx_2) is visible to the camera. For θ of 30° , the data throughput is reduced by 480 b/s for L of 60 cm, and only a 5-bit data stream (2-bit/ N_{channel} for Tx_1 and 3-bit for Tx_2), as shown in Fig. 12(b), is captured by the camera.

We have shown results for both setups in terms of the success rates of received bits, PSNR, and data throughput (e.g., a 100% success rate with a PSNR of ~ 14 and 17 dB were achieved for θ of 50° , L of up to 80 cm, and SS of 200 and 400 μs , respectively). Note that in this case, the f_{sf} was reduced by up to $\sim 50\%$ compared to the f_{sf} obtained in case of Tx without the inclusion of rotation. The maximum data throughputs of 1.9 and 0.9 kb/s were achieved at θ of 0° and 50° , respectively, for a L of up to 60 cm. A higher data throughput of 1.9 kb/s is observed for the transmission setup 1 due to the Tx units being located in the same plane; in the transmission setup 2, however,

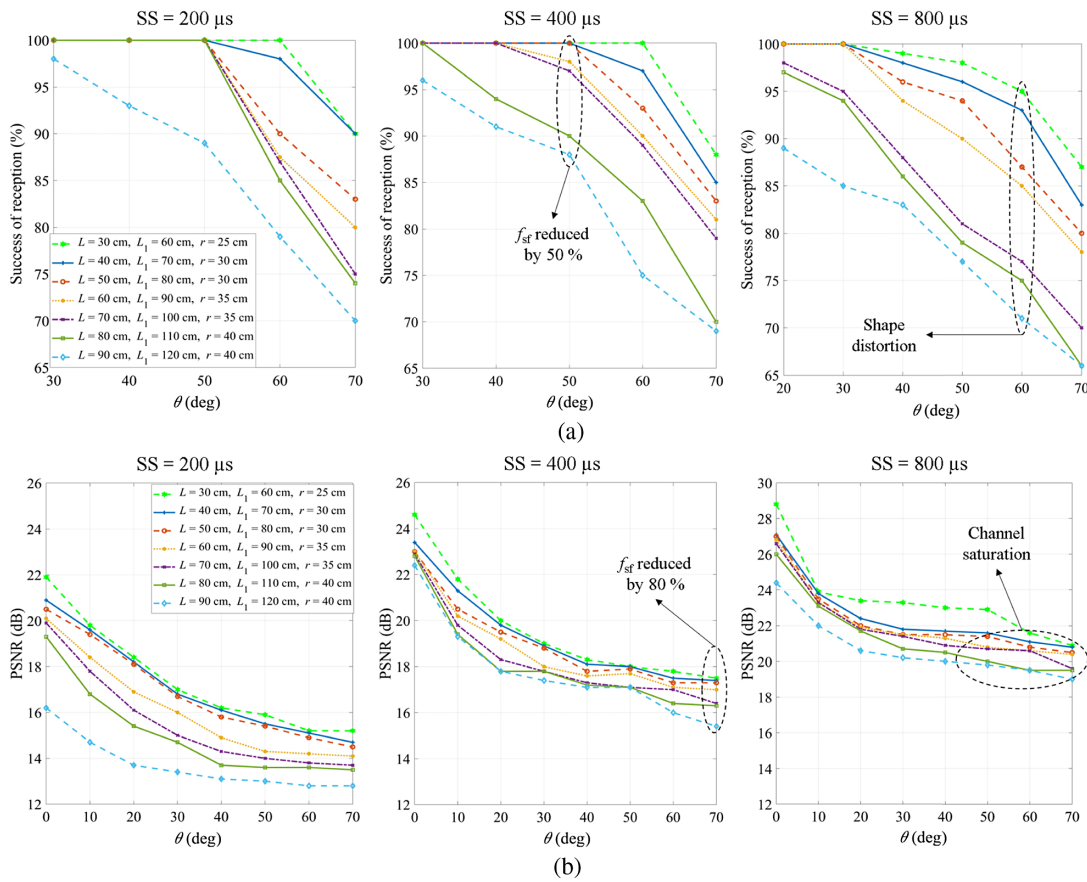


Fig. 13. Performance analysis: (a) success of reception and (b) PSNR.

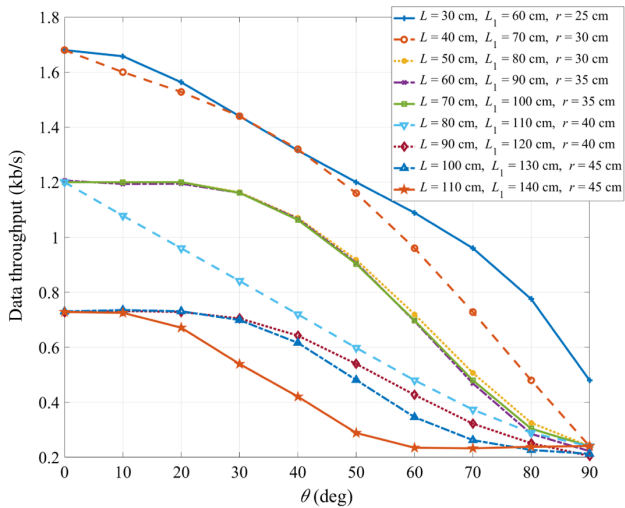


Fig. 14. Data throughput with respect to change in L and θ .

the data throughput is reduced to 1.68 kb/s as the Tx units are placed apart from each other at $(L_1 - L)$, as shown in Fig. 7(b). Therefore, the difference in the distances between the Tx units results in a decreased f_{sf} , which leads to a lower $N_{visible}$ and a reduced data throughput.

5. CONCLUSIONS

In this paper, we demonstrated f_{sf} -based angular behavior of multichannel MIMO-OCC for two different transmission setups where the Tx units are placed at different heights and distances from each other and the camera. We showed that the proposed study provided a 100% success rate in data reception at the optimum θ up to 50° for both the transmission setups at lower captured values of f_{sf} , which is projected onto the image sensor in the form of pixels. We provided a general solution based on f_{sf} to investigate the MIMO-OCC considering the angular movement of the Tx's. We believe the proposed study can be adopted for longer transmission distances based on f_{sf} and employing a Tx with a larger illuminating surface area for use in indoor environments [e.g., using Tx's with surface areas of $14 \times 14 \text{ cm}^2$, L can be extended to 1.6 m (i.e., $2 \times L$) and placing the Tx units at r of 80 cm apart can provide an optimum angle $\theta > 50^\circ$ for each case].

Unlike LOS and NLOS OCC links, the proposed system can be further adopted in indoor IoT-based links with multi-Tx's/Rx's and mobility, which offers an improved solution when consideration of the optimum angular orientation of multiple Tx units is critical. Although the small-scale experiments were only conducted for demonstration purposes, it is envisioned that the proposed study can readily be expanded using image processing techniques such as shape restoration using neural

networks and code extraction techniques to improve the success rate of received bits.

Funding. H2020 Marie Skłodowska-Curie Actions (764461).

Disclosures. The authors declare no conflicts of interest.

REFERENCES

- M. J. Jang, "15.7 amendment-optical camera communications study group (SG 7a)," IEEE 802.15 WPAN (2020).
- R. Boubezari, H. Le Minh, Z. Ghassemlooy, and A. Bouridane, "Smartphone camera based visible light communication," *J. Lightwave Technol.* **34**, 4121–4127 (2016).
- Z. Ghassemlooy, L. N. Alves, S. Zvanovec, and M.-A. Khalighi, *Visible Light Communications: Theory and Applications* (CRC Press, 2017).
- IEEE Standard for Local and Metropolitan Area Networks—Part 15.7: Short-range wireless optical communication using visible light, IEEE Standard 802.15.7-2011 (2011).
- C. Jurado-Verdu, V. Matus, J. Rabadan, V. Guerra, and R. Perez-Jimenez, "Correlation-based receiver for optical camera communications," *Opt. Express* **27**, 19150–19155 (2019).
- W. Huang, P. Tian, and Z. Xu, "Design and implementation of a real-time CIM-MIMO optical camera communication system," *Opt. Express* **24**, 24567–24579 (2016).
- M. Uysal, C. Capsoni, Z. Ghassemlooy, A. Boucouvalas, and E. Udvarý, "Optical camera communications," in *Optical Wireless Communications* (Springer, 2016), pp. 547–568.
- "IEEE 802.15. Documents TG7r1," 2020, <https://mentor.ieee.org/802.15/dcn/15/15-15-0746-01-007a-tg7r1-channel-model-document-for-high-rate-pdcommunications.pdf>.
- Panasonic news release, "Start the business of information collaboration services using the 'Hikari ID' technology," (in Japanese) <https://news.panasonic.com/jp/press/data/2015/12/jn151209-3/jn151209-3.html>.
- M. Shahjalal, M. K. Hasan, M. Z. Chowdhury, and Y. M. Jang, "Smartphone camera-based optical wireless communication system: requirements and implementation challenges," *Electronics* **8**, 913 (2019).
- S. R. Teli, S. Zvanovec, and Z. Ghassemlooy, "Performance evaluation of neural network assisted motion detection schemes implemented within indoor optical camera based communications," *Opt. Express* **27**, 24082–24092 (2019).
- S. R. Teli, V. Matus, S. Zvanovec, R. Perez-Jimenez, S. Vitek, and Z. Ghassemlooy, "Optical camera communications for IoT-rolling-shutter based MIMO scheme with grouped LED array transmitter," *Sensors* **20**, 3361 (2020).
- C.-W. Chow, C.-Y. Chen, and S.-H. Chen, "Visible light communication using mobile-phone camera with data rate higher than frame rate," *Opt. Express* **23**, 26080–26085 (2015).
- V. P. Rachim and W. Chung, "Multilevel intensity-modulation for rolling shutter-based optical camera communication," *IEEE Photon. Technol. Lett.* **30**, 903–906 (2018).
- W. Wang, C. Chow, C. Chen, H. Hsieh, and Y. Chen, "Beacon jointed packet reconstruction scheme for mobile-phone based visible light communications using rolling shutter," *IEEE Photon. J.* **9**, 1–6 (2017).
- V. Nguyen, Y. Tang, A. Ashok, M. Gruteser, K. Dana, W. Hu, E. Wengrowski, and N. Mandayam, "High-rate flicker-free screen-camera communication with spatially adaptive embedding," in *35th Annual IEEE International Conference on Computer Communications*, San Francisco, California, USA, 2016, pp. 1–9.
- K. L. Hsu, Y.-C. Wu, Y.-C. Chuang, C.-W. Chow, Y. Liu, X.-L. Liao, K.-H. Lin, and Y.-Y. Chen, "CMOS camera based visible light communication (VLC) using grayscale value distribution and machine learning algorithm," *Opt. Express* **28**, 2427–2432 (2020).
- Y. Yang, J. Hao, and J. Luo, "CeilingTalk: Lightweight indoor broadcast through LED-camera communication," *IEEE Trans. Mob. Comput.* **16**, 3308–3319 (2017).
- N. B. Hassan, Z. Ghassemlooy, S. Zvanovec, M. Biagi, A. M. Vegni, M. Zhang, and P. Luo, "Non-line-of-sight MIMO space-time division multiplexing visible light optical camera communications," *J. Lightwave Technol.* **37**, 2409–2417 (2019).
- N. B. Hassan, Z. Ghassemlooy, S. Zvanovec, P. Luo, and H. Le-Minh, "Non-line-of-sight 2 × N indoor optical camera communications," *Appl. Opt.* **57**, B144–B149 (2018).
- W.-C. Wang, C.-W. Chow, L.-Y. Wei, Y. Liu, and C.-H. Yeh, "Long distance non-line-of-sight (NLOS) visible light signal detection based on rolling-shutter-patterning of mobile-phone camera," *Opt. Express* **25**, 10103–10108 (2017).
- W. A. Cahyadi and Y. H. Chung, "Wide receiver orientation using diffuse reflection in camera-based indoor visible light communication," *Opt. Commun.* **431**, 19–28 (2019).
- C.-W. Chow, Z.-Q. Li, Y.-C. Chuang, X.-L. Liao, K.-H. Lin, and Y.-Y. Chen, "Decoding CMOS rolling-shutter pattern in translational or rotational motions for VLC," *IEEE Photon. J.* **11**, 1–5 (2019).
- Q. N. Pham, V. P. Rachim, J. An, and W.-Y. Chung, "Ambient light rejection using a novel average voltage tracking in visible light communication system," *Appl. Sci.* **7**, 670 (2017).
- F. de Souza Campos, J. A. C. Ulson, J. W. Swart, M. J. Deen, O. Marinov, and D. Karam, "Temporal noise analysis and measurements of CMOS active pixel sensor operating in time domain," in *26th Symposium on Integrated Circuits and Systems Design (SBCCI)*, Curitiba, Brazil, 2013, pp. 1–5.
- Q. Wang, Y. Shen, and J. Jin, "Performance evaluation of image fusion techniques," in *Image Fusion* (Academic, 2008), pp. 469–492.
- J. Price and T. Goble, "Signals and noise," in *Telecommunications Engineer's Reference Book*, F. Mazda, ed. (Butterworth-Heinemann, 1993), pp. 1–15.
- P. Burgess, "WS2812B: Intelligent control LED integrated light source," in *Adafruit NeoPixel Uberguide*, <https://cdn-shop.adafruit.com/datasheets/WS2812B.pdf>.
- M. D. Thieu, T. L. Pham, T. Nguyen, and Y. M. Jang, "Optical-Rol-signaling for vehicular communications," *IEEE Access* **7**, 69873–69891 (2019).
- C. Xiu and R. Wang, "Hybrid tracking based on camshift and template matching," in *29th Chinese Control and Decision Conference (CCDC)*, Chongqing, China, 2017, pp. 5753–5756.
- Visible Light Communication*, Shlomi Arnon, ed. (Cambridge University, 2015).
- Atmel Corporation, "8-bit Microcontroller with 4/8/16/32K bytes in-system programmable flash," (2009), <https://www.sparkfun.com/datasheets/Components/SMD/ATMega328.pdf>.
- Sony Corporation, "IMX219PQH5-C Datasheet," 2020, <https://datasheetspdf.com/pdf/1404029/Sony/IMX219PQH5-C/1>.